INTERNATIONAL JOURNAL FOR NUMERICAL METHODS IN BIOMEDICAL ENGINEERING
Int. J. Numer. Meth. Biomed. Engng. (2012)
Published online in Wiley Online Library (wileyonlinelibrary.com). DOI: 10.1002/cnm.2511

Patient-specific finite element analysis of carotid artery stenting: a focus on vessel modeling

F. Auricchio, M. Conti*,†, A. Ferrara, S. Morganti and A. Reali

Department of Civil Engineering and Architecture, Structural Mechanics Division, University of Pavia, Via Ferrata 1, 27100 Pavia, Italy

SUMMARY

Finite element analysis is nowadays a well-assessed technique to investigate the impact of stenting on vessel wall and, given the rapid progression of both medical imaging techniques and computational methods, the challenge of using the simulation of carotid artery stenting as procedure planning tool to support the clinical practice can be approached. Within this context, the present study investigates the impact of carotid stent apposition on carotid artery anatomy by means of patient-specific finite element analysis. In particular, we focus on the influence of the vessel constitutive model on the prediction of carotid artery wall tensional state of lumen gain and of vessel straightening. For this purpose, we consider, for a given stent design and CA anatomy, two constitutive models for the CA wall, that is, a hyperelastic isotropic versus a fiber-reinforced hyperelastic anisotropic model. Despite both models producing similar patterns with respect to stress distribution, the anisotropic model predicts a higher vessel straightening and a more evident discontinuity of the lumen area near the stent ends as observed in the clinical practice. Although still affected by several simplifications, the present study can be considered as further step toward a realistic simulation of carotid artery stenting. Copyright © 2012 John Wiley & Sons, Ltd.

Received 8 June 2011; Revised 25 July 2012; Accepted 13 August 2012

KEY WORDS: finite element analysis (FEA); carotid artery stenting (CAS); patient-specific modeling

1. INTRODUCTION

Carotid artery stenting (CAS) is a minimally invasive procedure aiming at overcoming carotid artery (CA) stenosis by balloon angioplasty followed by the apposition of a metallic stent, to avoid acute vessel re-narrowing. CAS has emerged as an acceptable counterpart of the surgical approach, that is, carotid endarterectomy [1]. However, the long-term efficacy of CAS is currently under clinical evaluation and, in particular, the role of in-stent restenosis (ISR) is still unclear. ISR is a well-known drawback of stenting and consists of the post-stenting lumen renarrowing due to neointimal hyperplasia, that is, abnormal increase of the endotelium cells. Even though such a problem is deeply investigated and treated with novel drug-eluting technology for coronary stenting [2], few and contrasting data are available for CAS as discussed in the following. In 2005, Gröschel *et al.* [3] stated that the assessment of ISR rate of CAS is challenging. In fact, they performed a systematic meta-analysis of all current peer-reviewed studies about CAS ISR, highlighting a wide range of ISR rate (from 0.6% [4] to 20.8 % [5]). They also remarked that such a variability could be due to a low standardization of the ISR rate computation, which indeed depends on several issues such as adopted restenosis threshold, follow-up term, study design, and others.

In the same year, Bosiers *et al.* [6] reported CAS data, collected in 5 years by four high-volume European centers (ELOCAS registry), indicating a restenosis rate of 1%, 2% and 3.4% after 1, 3 and 5 years, respectively.

*Correspondence to: Michele Conti, Department of Civil Engineering and Architecture, Structural Mechanics Division, University of Pavia, Via Ferrata 1, 27100 Pavia, Italy.

†E-mail: michele.conti@unipv.it

In 2008, De Donato *et al.* [7] carried out a retrospective investigation on 3179 CAS procedures, performed from 1998 to 2006, aiming at evaluating the long-term CAS outcomes; the data indicate an ISR rate of 1.6%, 3.9% and 6% after 1, 3 and 5 years, respectively; consequently, they concluded that ISR for CAS appears to be acceptable and unrelated to device characteristics.

In the same year, Steinbauer *et al.* [8] analyzed the results of a prospective, randomized, single-center study revealing a high incidence (18.75%) of relevant ISR ($\geq$ 70%), but, in this case, it is necessary to underline that only one type of stent, that is, Wallstent (Boston Scientific Co., Natick, MA, USA), was used. A high rate of ISR also appears from the data reported in the same period by Harrer *et al.* [9] and more recently by Nolz *et al.* [10].

Although we are not reporting all the available studies and literature reviews, it is evident that the clinical relevance of CAS ISR is still a matter of debate, and it could become more prevalent because of the exponential growth of CAS procedures. As a consequence, more data and dedicated studies are necessary to illustrate the mechanisms of ISR and their relation with the novel technologies rapidly emerging in the CAS procedure. In this context, computational biomechanics can play a key role in investigating the relation between biomechanical factors and the development of ISR. In fact, starting from the experimental evidence that restenosis and neointimal hyperplasia are related to vessel wall injury [11–13], many studies have analyzed the impact of stent deployment or angioplasty on vessel wall stress distribution through finite element analysis (FEA), just to name a few [14–18]. However, the major part of these studies deals with coronary stenting, and only few focus on CAS [19–22].

Wu *et al.* [19] considered two different stents to show the influence of stent design on the stent-vessel interactions. Despite the fact that this study addresses the delivery and the expansion simulation of nitinol stent in a tortuous anatomy, the authors adopted idealized geometries for both stent and vessel anatomy. Moreover, an isotropic hyperelastic model has been considered for vessel wall on the basis of the data reported by Lee *et al.* [23], which can not be explicitly referred to human carotid artery.

Auricchio *et al.* [21] used FEA to evaluate the performance of three commercially available self-expanding stents, in different sizes and configurations, in a patient-specific CA model based on computed angiography tomography images; this study was further extended [22] to investigate the role of stent design on vessel scaffolding comparing FEA with experimental data. Although in these studies realistic geometries for both stent and vessel are considered, the mechanical response of the vessel wall was still reproduced through isotropic, homogeneous hyperelastic material model, and the adopted material constants were derived from the study of Lally *et al.* [15], who dealt with human femoral artery.

Both studies are modeling CA tissue as an isotropic, homogeneous hyperelastic material for the sake of simplicity, but the experimental evidence suggests that the mechanical response is anisotropic and varies along the vessel [24]. Moreover, the vessel wall is not a homogeneous material because of the presence of the plaque between the layers.

Moving from these considerations, the present study aims at evaluating the impact of vessel constitutive modeling on the outcomes of CAS simulation, such as CA wall tensional state, lumen gain, and vessel straightening. In particular, we consider two possible constitutive models: (i) hyperelastic isotropic and (ii) fiber-reinforced hyperelastic anisotropic [25, 26].

The study is organized as follows: we first discuss the generation of the patient-specific model of CA, which includes the plaque and is based on computed tomography angiography (CTA) DICOM images; we then detail and justify the selection of the adopted constitutive models for the vascular tissue; we finally illustrate the post-processing of the simulation outputs, discussing the results.

2. MATERIALS AND METHODS

Because this study focuses on the stent implantation, we include the following parts in our simulation:

- a patient-specific CA model;
- the stent model;
- the catheter model.

DOI: 10.1002/cnm

The numerical analysis is clearly non-linear, involving large deformations and contact; we use Abaqus/Explicit (Simulia, Dassault Systèmes, Providence, RI, USA) as finite element solver (Section 2.4). In the following, we discuss the CA and stent model, the FEA settings and the post-processing of the numerical results.

2.1. Carotid artery model: geometry and mesh

We base the CA model on DICOM images of a neck–head CTA performed on a 70-year-old female patient. The CTA scan is performed at IRCCS San Matteo in Pavia, Italy, using a Somatom Sensation Dual Energy scanner (Siemens Medical Solutions, Forchheim, Germany). The scan data are characterized by the following features: slice thickness, 1 mm; slice width × height, 512 × 512 pixels; pixel spacing, 0.33 mm.

We elaborate the images using OsiriX [27] (Figure 1(a)); in particular, we focus on the left CA and, exploiting the thresholding of the Hounsfield unit scale, we highlight both the bifurcation lumen and the plaque as shown in Figure 1(b). We then export the 3D surfaces of both lumen and plaque geometry in stereolithography (STL) format, that is, as a set of connected triangles (Figure 2(a)).

To create the CA finite element mesh, we implement in Matlab (The Mathworks Inc., Natick, MA, USA) a procedure composed of four main steps:

1. definition of vessel wall inner profile elaborating the STL surface of the lumen;
2. definition of vessel wall outer profile from the inner profile;
3. generation of the mesh between the inner and outer profile;
4. identification of a subset of vessel wall elements defining the plaque.

In the first step, we define the vessel wall inner profile from the CA lumen STL surface (Figure 2(a)), which is processed to define a given number of closed lines representing the cross-sectional profile of each CA bifurcation branch (i.e., common carotid artery (CCA), internal carotid artery (ICA), external carotid artery (ECA)), as shown in Figure 2(b).

In the second step, because no information on vessel wall thickness is obtainable from CTA images, we reconstruct the vessel wall outer profile (Figure 2(c)) enlarging the inner sections to

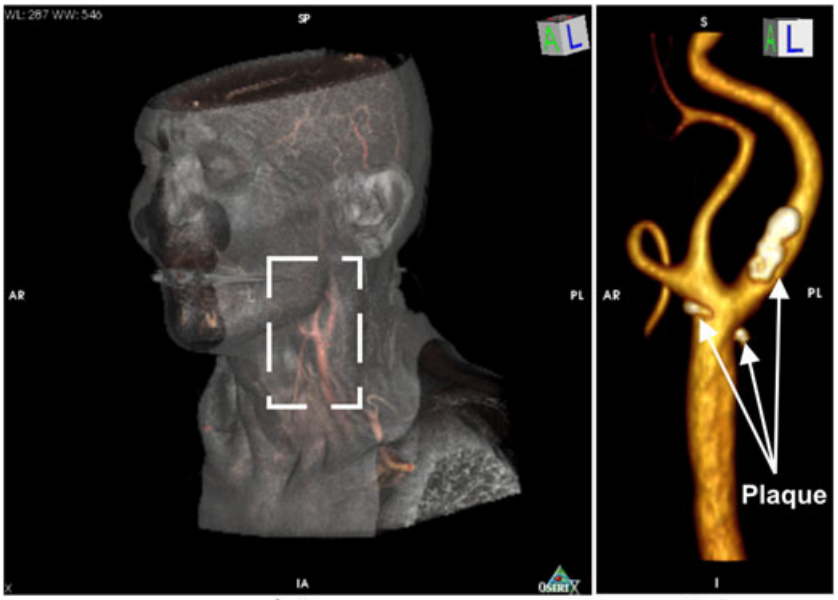

Figure 1. Elaboration of computed tomography angiography images: (a) whole 3D reconstruction of neck–head district highlighting the region of interest; and (b) 3D reconstruction of both lumen of left carotid artery bifurcation and plaque (white).

DOI: 10.1002/cnm

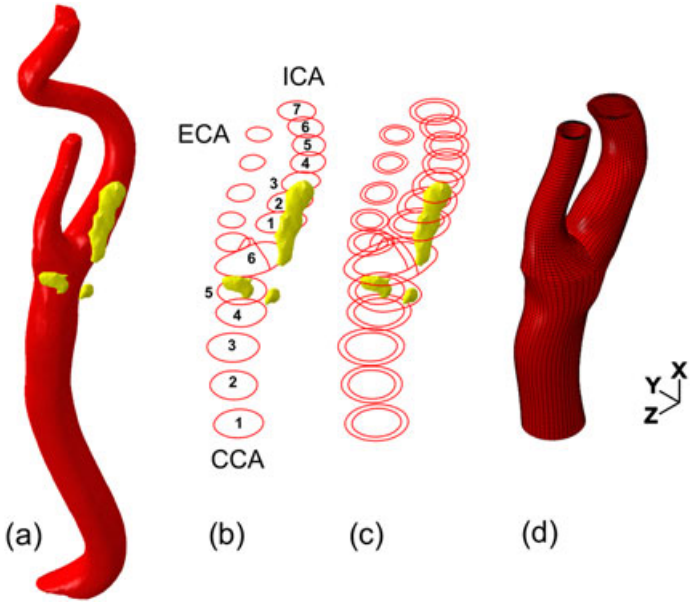

Figure 2. Generation of carotid artery wall mesh: (a) 3D reconstruction of vessel lumen and plaque; (b) closed lines representing the inner cross-sectional profile; (c) closed lines representing the inner and outer cross-sectional profiles; and (d) carotid artery wall mesh.

maintain the plaque enclosed between the inner and outer profile. In fact, for each section, we define a local cylindrical coordinate system, with the origin located in the section center of mass; then, for each section point, we impose a radial shift corresponding to the vessel wall thickness, which is defined as a percentage of the radius (i.e., 28.19% for CCA and 32.31% for ICA and ECA, as suggested by Sommer *et al.* [24]) for the regions where there is no plaque, and appropriately increased for the regions where the plaque is present. Representative examples of this procedure are depicted in Figure 3, whereas the wall thickness, as a function of the CA sections, is reported in Table A.1 of the Appendix.

In the third step, once both inner and outer sections are defined, we interpolate separately both of them along the longitudinal direction with cubic splines defining thus the inner and outer boundary of the model; we then connect such boundaries to define a hexahedral-element mesh (Figure 2(d)).

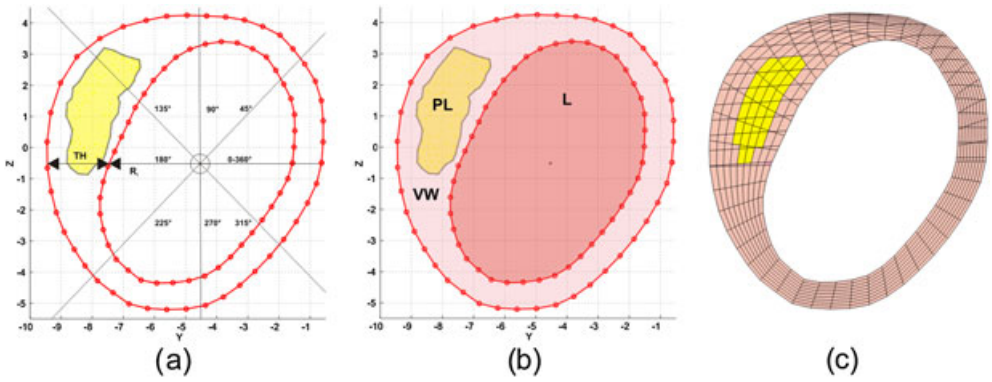

Figure 3. Representative example of the vessel wall definition (ICA section 1): (a) reconstruction of outer vessel wall profile; (b) obtained lumen, L (red)-, vessel wall, VW (pink)- and plaque, PL (yellow)-; (c) cut-view of the obtained mesh.

DOI: 10.1002/cnm

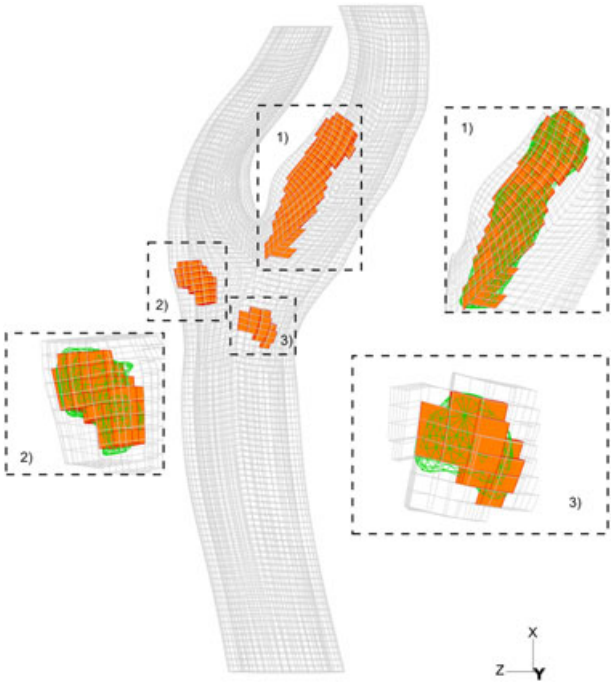

Figure 4. Inclusion of the plaque in the carotid artery vessel model: the plaque (orange) is defined assessing the elements of the vessel wall mesh (gray) enclosed within 3D stereolithography surface (green) representing the plaque morphology.

In the final step, we define the plaque as a subset of vessel wall elements, which are enclosed within the 3D STL surface of the plaque. Consequently, it is possible to divide the whole CA element set into two subsets of elements representing respectively the CA wall and the plaque, as depicted in Figure 4.

The proposed procedure is repeated generating a series of meshes, with different element sizes, used to perform a preliminary mesh-convergence analysis resulting in an optimal CA mesh defined by 59,346 elements and 66,560 nodes, as described in the Appendix.

2.2. *Carotid artery model: constitutive laws*

Constitutive modeling of arterial tissue is not a trivial task because of its biological complexity. It can be considered as a composite material defined by three layers (i.e., intima, media, and adventitia), with anisotropic components (i.e., stiff collagen fibers with a given orientation and dispersion) immersed in an isotropic matrix where highly stretchable elastin is predominant. Such structural complexity results in a non-trivial mechanical behavior, which can be described by the following main aspects: (i) high non-linear response; (ii) anisotropy; (iii) small hysteresis; and (iv) nonlinear stiffening, especially at high levels of strain, due to the progressive recruitment of collagen fibers. Moreover, if we consider *in vivo* condition, the arterial wall is pre-stretched (because of blood pressure loading) and in an activated state (because of nervous stimuli acting on the smooth muscle cells); furthermore, the arterial load-free configuration is characterized by residual stresses both in circumferential and axial direction.

Several constitutive models of arterial tissue, with different degrees of complexity, are available in the literature, usually based on the continuum theory of large deformation elasticity and described by a strain energy function (SEF), which defines the energy stored in the material as a function of the deformation. Once the SEF is defined, it is necessary to calibrate its parameters on experimental data obtained from tissue samples, but, because experimental data of the mechanical properties of arterial tissue are not easy to achieve, the constitutive model calibration is complex in most cases.

DOI: 10.1002/cnm

Because we aim at investigating the role of vessel wall constitutive modeling with respect to different post-stenting features, we choose to deal with only two constitutive models for the vessel tissue, although we adopt the same model for the plaque. Each vessel constitutive model resembles different features and levels of complexity:

1. *model HI* - homogeneous, single-layer, isotropic model: it does not differentiate the mechanical behavior of the CA branches (i.e., CCA and ICA/ECA) and does not take into account the layered structure of the vessel wall and its anisotropic mechanical behavior;
2. *model HA* - non-homogeneous, single-layer, fiber-reinforced anisotropic model: it takes into account the anisotropic behavior of the vessel wall and differentiate the mechanical response of carotid branches, that is, CCA and ICA/ECA.

For model HI the adopted strain energy function reads as follows:

$$\Psi = \sum_{i+j=1}^{2} C_{ij}(I_1 - 3)^i (I_2 - 3)^j, \tag{1}$$

where C_{ij} are material parameters, whereas I_1 and I_2 are the first and second invariant of the right Cauchy–Green deformation tensor, $\mathbf{C}$, defined as

$$I_1 = \operatorname{tr} \mathbf{C}, \qquad I_2 = \frac{1}{2}\left[I_1^2 - \operatorname{tr} \mathbf{C}^2\right]. \tag{2}$$

The material coefficients are taken from Creane *et al.* [28], who refer to the studies of Gao *et al.* [29] and Tang *et al.* [30] for the CA wall material model constants.

For model HA, accounting for two families of fibers, the adopted strain energy function [25, 26] reads as follows:

$$\Psi = C_{10}(I_1 - 3) + \frac{k_1}{2k_2} \sum_{i=4,6} \left\{\exp\left[k_2(\kappa I_1 + (1 - 3\kappa) I_i - 1)^2\right] - 1\right\}, \tag{3}$$

where C_{10}, k_1, k_2, κ are material coefficients, whereas I_4 and I_6 are invariants measuring the square of the stretch along the direction of the fibers [25, 26]. The parameter κ describes the dispersion of a given fiber family, with a value ranging from 0 to $1/3$; in particular, $\kappa = 0$ implies that there is no dispersion and the fibers are perfectly aligned, whereas $\kappa = 1/3$ implies that the fibers are randomly distributed and the material is thus isotropic.

In this work, we obtain the material coefficients by appropriate fitting of the anisotropic strain energy function (Equation (3)) on the experimental data of extension–inflation tests recently reported by Sommer *et al.* [24, 31], who have systematically determined the biaxial mechanical properties of human CCAs and ICAs (in intact and layer-dissected status) by quasi-static extension–inflation tests at different axial stretches. For the sake of simplicity we refer only to data of intact walls.

The calibration is carried out through a standard optimization technique defining the objective function χ^2 as the squared sum of the residuals, that is, the difference between the experimental measurements and the corresponding calculated variables:

$$\chi^2 = \sum_{a}^{N} \left[\frac{1}{w_1^2} \left(p_i^{\Psi} - p_i^{exp}\right)_a^2 + \frac{1}{w_2^2} \left(F_z^{\Psi} - F_z^{exp}\right)_a^2 \right], \tag{4}$$

where w_1 and w_2 are weights, p_i, F_z are respectively the inner pressure and axial force. Superscripts Ψ, exp stand respectively for model prediction and experimental measurements. The results of the fitting procedure are illustrated in Figure 5, whereas the obtained model coefficients are reported in Table I. It is worth to highlight that to differentiate the mechanical response of the carotid branches, we split the vessel mesh in two subregions, that is, CCA and ICA/ECA, assuming thus ICA and ECA have the same mechanical behavior. Moreover, despite the fact that the parameter κ can be derived from histological measurements or considered as a parameter to include in the material model calibration, we assume $\kappa = 0$ for the sake of simplicity.

DOI: 10.1002/cnm

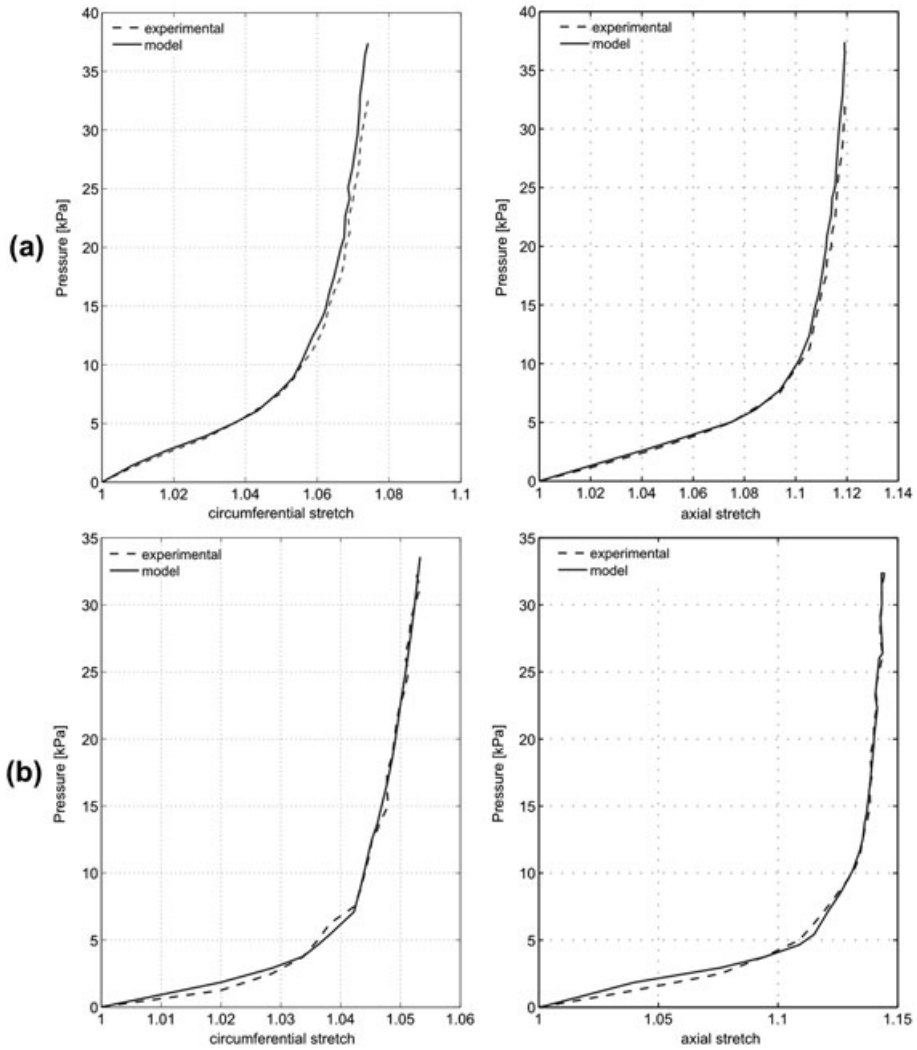

Figure 5. Constitutive models and data fitting: model prediction versus the experimental data reported by Sommer *et al.* [24] for (a) internal carotid arteryand (b) common carotid artery intact wall.

Table I. Constitutive parameters of the adopted strain energy functions in the two model variants.

Model label	Vessel		Plaque	
HI	$C_{10} = 50.45$ kPa $C_{01} = 30.49$ kPa $C_{20} = 40$ kPa $C_{11} = 120$ kPa $C_{02} = 10$ kPa	Reference: Creane *et al.* [28] SEF: Equation (1)	$C_{10} = 4.8$ kPa $C_{01} = 60$ kPa $C_{20} = 240$ kPa $C_{11} = 377$ kPa $C_{02} = 781$ kPa	Reference: Creane *et al.* [28] strain energy function: Equation (1)
HA	CCA - Wall $C_{10} = 24.43$ kPa $k_1 = 1.66$ kPa $k_2 = 111.4$ $\gamma = 47.89°$	ICA - Wall $C_{10} = 13.72$ kPa $k_1 = 0.52$ kPa $k_2 = 195.32$ $\gamma = 33.78°$		see model *HI*
	Reference: Sommer *et al.* [24]; strain energy function: Equation (3)			

SEF, strain energy function; CCA, common carotid artery; ICA, internal carotid artery.

DOI: 10.1002/cnm

With respect to the plaque, we assume an isotropic behavior described by the strain energy function of Equation (1) as proposed by Creane *et al.* [28], and we refer to the material coefficients therein reported; in this study, the authors investigated the plaque vulnerability by FEA, deriving the material model constants from mechanical testing of excised carotid plaque reported by Maher *et al.* [32].

Both strain energy functions (Equations (1) and (3)) are available in the material library of Abaqus v. 6.9 [33]; in the case of anisotropic model the assignment of local reference system is required for each element to define the relative fiber orientation, and therefore, we developed a dedicated subroutine in Matlab, as described in Appendix A.3.

2.3. Stent model

We consider a 9-mm Bard ViVEXX Carotid Stent (C. R. Bard Angiomed GmbH & Co., Germany), an *open-cell* self-expanding Nitinol stent with a straight configuration.

A model based on high resolution (5 μm) micro-CT scans of the real device (Figure 6) and a final mesh consisting of 93,024 C3D8R elements and 171,720 nodes is adopted.

To reproduce the superelastic material response, we use the Abaqus user material subroutine [34] of the superelastic model originally proposed by Auricchio and Taylor [35, 36]. The adopted Nitinol constitutive parameters are those reported in [37], whereas the density is assumed to be 6.7 g/cm^3.

2.4. Finite element analysis of carotid artery stenting

As previously stated, the simulation of CAS is performed assembling the following parts:

- a patient-specific CA model;
- the stent model;
- the catheter model.

The catheter is modeled as a rigid body defined by a surface obtained by sweeping a cylindrical section along the centerline of the vessel; we mesh it with 2760 three-dimensional, four-node surface elements with reduced integration (SFM3D4R).

In our simulation strategy, the stent deformation is driven by the configuration change of the catheter, imposed by displacement boundary conditions on its nodes, determined as the difference between a starting and final catheter configuration for each simulation step. In particular, the simulation consists of two steps:

1. Stent crimping and bending: starting from a straight configuration, the catheter is gradually bent and crimped following the vessel centerline and leading to the stent deformation; the contact between the stent and the vessel is deactivated in this step;
2. Stent deployment: from the bent and crimped configuration, the catheter is re-enlarged and the stent expands against the vessel wall; the contact between the stent and the vessel is activated in this step.

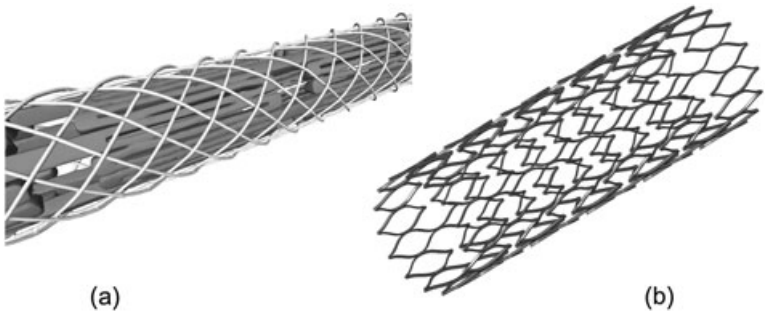

Figure 6. a) three-dimensional reconstruction of an 8.45-mm portion of the stent (dark gray) within the delivery sheath (light gray); b) finite element model of the open-cell stent in free expanded configuration.

DOI: 10.1002/cnm

We run two different simulations; one for each considered CA constitutive model. Each simulation is performed using Abaqus/Explicit v. 6.9 as finite element solver because the numerical analysis is characterized by non-linearity because of the material properties, large deformations and complex contact problems.

At the vessel ends, we define *ad hoc* local cylindrical coordinate systems to fix the corresponding nodes in the longitudinal and in the circumferential direction allowing thus only radial displacements. Moreover, the longitudinal displacement of the nodes lying at the proximal end of the stent are restrained to maintain the longitudinal position of the stent equal for all the simulations.

We assume no internal pressure on the vessel wall under the hypothesis that the geometry is based on measurements achieved at 80 mmHg. Finally, a frictionless contact between the stent and the vessel inner surface is assumed.

2.5. Post-processing

We evaluate the impact of each constitutive vessel model on the simulation results focusing on the following aspects:

- Evaluation of von Mises stress σ_M[‡] distribution in the post-stenting vessel, as a measure of potential injury induced by the stent apposition to the vessel;
- Comparison of the pre-stenting and post-stenting lumen area; we consider the distal (i.e., ICA) and proximal (i.e., CCA) end of the stented region;
- Computation and comparison between the pre-stenting and post-stenting vessel tortuosity [21, 38], as a measure of the vessel straightening induced by the stent insertion.

Despite the fact that σ_M is generally adopted as a plasticity criterion, in the present study, σ_M is considered as a scalar map of a complex 3D tensional state, following the approach of other similar studies [29, 39, 40] investigating the impact of vascular implants on vessel wall. We elaborate σ_M to define the three following indices:

- σ_M^{Max}: the maximum value of σ_M with respect to all CA elements;
- $\sigma_M^{99\mathrm{P}}$: this index corresponds to the cut-off σ_M value at 99% of the cumulative histogram with respect to pre-stenting vessel volume (i.e., only 1% of the volume has σ_{Mises} above $\sigma_M^{99\mathrm{P}}$);
- σ_M^{Mean}: this index is defined as $\sigma_M^{\mathrm{Mean}} = \sum_{i=1}^{N} \sigma_{M_i} V_i / \sum_{i=1}^{N} V_i$ where V_i is the element volume and N is the number of elements whose σ_M is above 0.1 kPa.

From a qualitative point of view, we also consider the distribution over the vessel inner surface of σ_M and maximum principal stress, as we want to check whether the localization of the high-stress regions with respect to CA anatomy is independent of the material model.

3. RESULTS AND DISCUSSION

One simulation for each considered CA constitutive model is performed and, as an illustrative example of the final result, we depict in Figure 7 the vessel, the stent, and the catheter configuration during CAS simulation for model HA.

The three stress indices, that is, σ_M^{Max}, $\sigma_M^{99\mathrm{P}}$ and σ_M^{Mean} for CA wall as a function of the two adopted constitutive models are reported in Table II. All the indices obtained using the isotropic model (HI) are higher than when fibers are present (model HA), in fact, post-stenting stress of the vessel wall predicted by anisotropic model is 30–40% lower than the isotropic counterpart (Table II). This result is somehow coherent with the outcomes of the study by Holzapfel *et al.* [41], who investigated, among other model features, the impact of material anisotropy on the resulting stress distributions in balloon angioplasty. In fact, they concluded that a model simplification such

[‡]The von Mises stress σ_M (or equivalent stress) is a scalar quantity resuming the tensional state represented by the second-order stress tensor $\boldsymbol{\sigma}$; $\sigma_M = \sqrt{\frac{3}{2}\mathbf{S}:\mathbf{S}}$, where $\mathbf{S}$ is the deviatoric stress tensor, defined as $\mathbf{S} = \boldsymbol{\sigma} - p\mathbf{I}$, where $p = tr(\boldsymbol{\sigma})$ is the pressure stress.

DOI: 10.1002/cnm

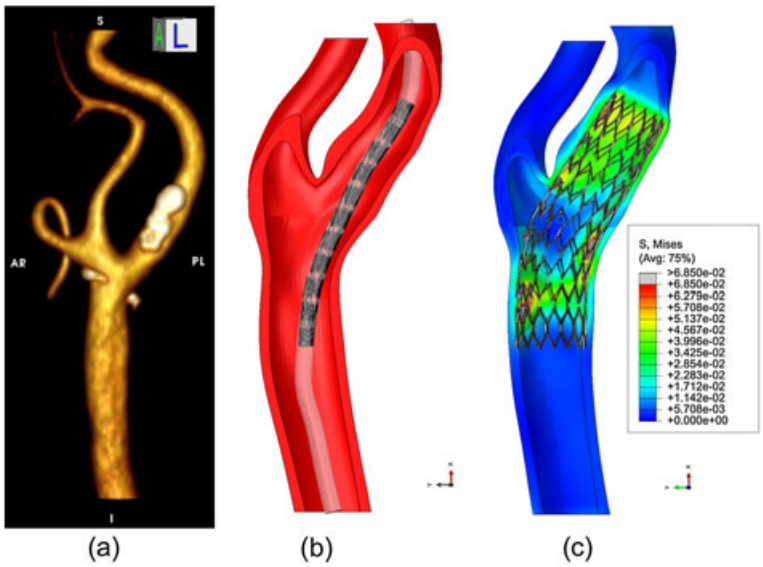

Figure 7. Finite element analysis of carotid artery stenting: (a) 3D reconstruction of carotid artery lumen from computed tomography angiography images; (b) stent crimped in the delivery system during the simulation; (c) contour plot depicting the post-stenting stress distribution over the vessel wall (model HA) at the end of the simulation; the cut-view option is used for the vessel and MPa is the unit of measure for σ_M.

Table II. Stress indices [kPa] as function of the adopted carotid artery models.

Model label	*HI*	*HA*	*HA* versus *HI* [%]
σ_M^{Max}	152.4	91.3	−40
$\sigma_M^{99\mathrm{P}}$	96.5	60.6	−37.2
σ_M^{Mean}	14.3	9.5	−33.5

as adopting an isotropic model, can lead to a significant mismatch (up to 600%) with the reference anisotropic model. Anyway, the authors underlined that there are no straightforward explanations for these results because they are caused by a complex interaction of several factors such as a generally higher compliance at large strains.

If we focus on the magnitude of our computed post-stenting stress reported in Table II and exclude σ_M^{Max}, which can be affected by local stress concentrations, the range of $\sigma_M^{99\mathrm{P}}$ is 60.6–96.5 kPa, whereas the range of σ_M^{Mean} is 9.5–14.3 kPa. Such values fall within the stress ranges reported by similar numerical studies on CA, available in literature [29, 42–45], but such a comparison is not trivial as material models, stress indices, and loading conditions are, in general, different. In particular, narrowing the comparison to the studies addressing the CAS simulation, Wu *et al.* obtained first principle stresses of the vessel caused by the stent apposition ranging from 74 to 99 kPa, whereas Auricchio *et al.* [21] reported values of $\sigma_M^{99\mathrm{P}}$ ranging from 94 to 309 kPa, highlighting the dependency of post-stenting vessel wall stress on stent design and configuration.

Because the stress magnitude depends on several items, the *per se* consideration of this value is not completely meaningful if not supported by an indication of its distribution over the vessel wall, which can be considered as a map of the stent-induced injury, driving the ISR.

For this reason, we report in Figure 8 the contour plot of the post-stenting σ_M, maximum principal stress and contact pressure. The results highlight the complex stress distribution induced by the stent apposition, which is indicated by both considered constitutive models. In particular, if we

DOI: 10.1002/cnm

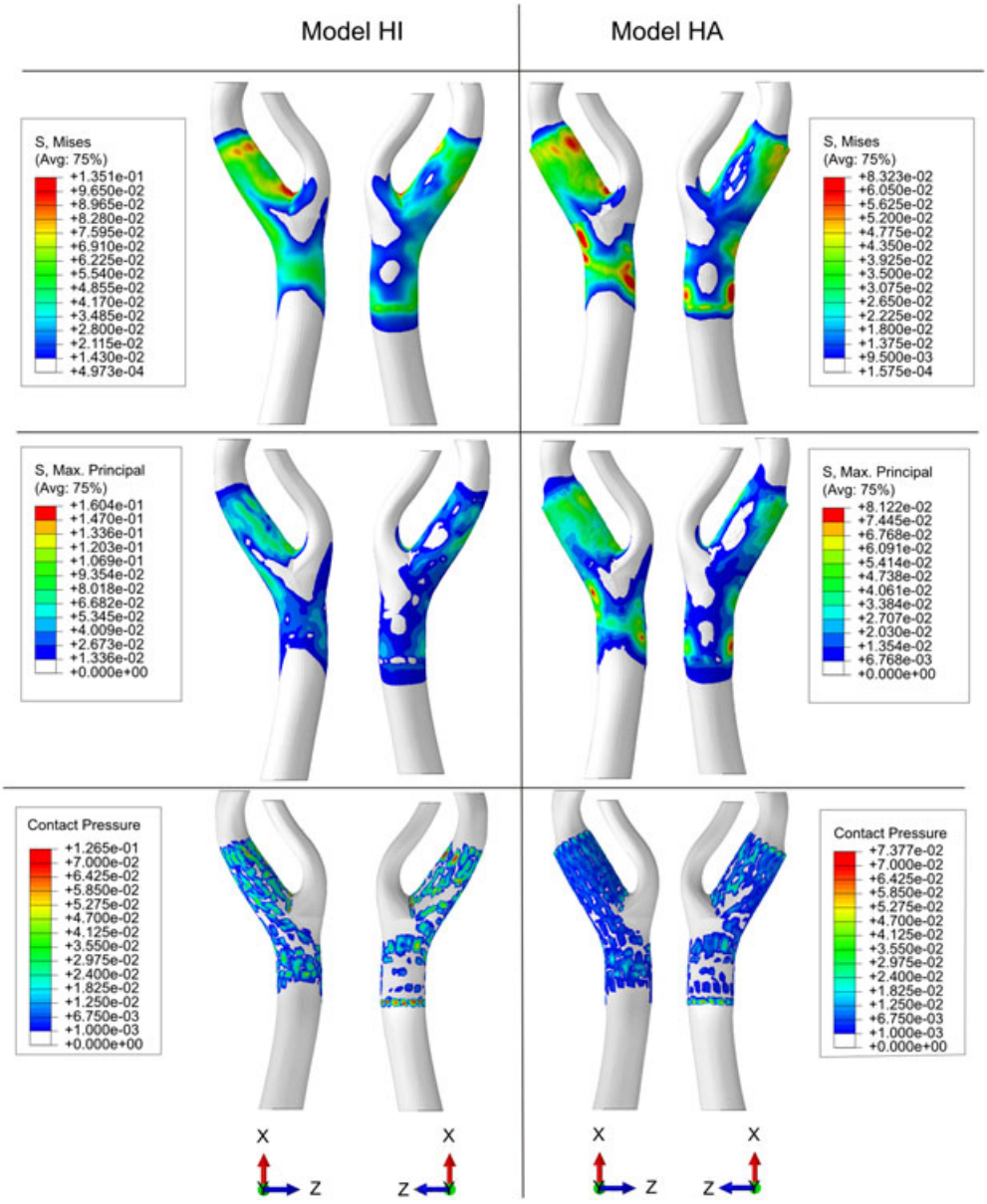

Figure 8. Post-stenting σ_M (top), maximum principal stress (middle) and contact pressure (bottom) distribution over the inner vessel wall (front and back views). With respect to σ_M, the color bar is rescaled by setting the corresponding $\sigma_M^{99\mathrm{P}}$ as the maximum and σ_M^{Mean} as the minimum. MPa is the unit of measure.

consider the σ_M contour plot depicted in Figure 8(top), it is possible to identify three different high-stress regions located at the distal and proximal ends of the implant and on the inner part of the bifurcation. Nevertheless, the impact of the stent on the proximal end, that is, on CCA branch, is more evident in model HA than in model HI.

Moreover, if we consider CCA and ICA branches separately, both models predict σ_M^{Mean} of ICA almost 70% higher than σ_M^{Mean} of CCA (i.e., ICA-HA: 15.4 kPa, CCA-HA: 9.0 kPa, ICA-HI: 23.4 kPa, CCA-HI: 14 kPa), thus indicating a higher solicitation of ICA branch. These considerations are matching the experimental results reported by Clark *et al.* [46], who assessed CAS ISR by intravascular ultrasound imaging. In fact, they found the greatest amount of neointima at lesion site of the ICA; the authors explain such results linking the stent oversizing with chronic expansile force, which leads ongoing injury to deep wall and hence promotes greater neointima. Our results

DOI: 10.1002/cnm

are thus suggesting the following: (i) that stress is not uniformly distributed, (ii) that high-stress areas are located at the stent ends and (iii) that the ICA branch is more stressed than CCA branch.

Additionally, we report in Table III the values of the pre-stenting and post-stenting lumen and tortuosity, whereas in Figure 9, a representative illustration of the pre-stenting and post-stenting lumen profile and centerline is presented. Even though the prediction of post-stenting lumen for CCA is similar in both cases, the anisotropic model indicates a higher vessel straightening and a significant lumen enlargement of the ICA. With respect to vessel straightening and lumen enlargement, it is worth highlighting that the use of a fiber-reinforced anisotropic model, differentiating ICA and CCA tissue, allows to predict a significant lumen enlargement near the stent ends, as observed in the clinical practice (Figure 10).

Despite the fact that FEA of stenting can be considered nowadays, a routine in computational biomechanics, the challenge of using simulations in clinical practice, still requires further research effort. In the present study, we move a step forward with respect to the available literature as we introduce three main novelties: (i) inclusion of the plaque morphology, derived from medical images in the carotid artery model; (ii) use of fiber-reinforced anisotropic hyperelastic model; (iii) calibration of the anisotropic model on the data recently reported by Sommer *et al.* [24], who have systematically determined the mechanical properties of human CCAs and ICAs, in intact and layer-dissected status. Given these data, we differentiate the mechanical response of the vessel distinguishing between ICA/ECA and CCA branches.

Clearly, one of the main issues to bring such simulations from research to practice is the computational cost; our results indicate that in optimizing the hardware use, it is possible to finalize the analysis in 11 h using 8 CPUs (Appendix A.4); despite the fact that it is very far from the ideal on-fly response, this result shows the feasibility of performing an analysis in an acceptable time to support procedure planning. In fact, usually 1 week is the time elapsed between the diagnostic imaging and CAS performance. From a broader point of view, the performance of realistic stenting simulations as

Table III. Pre-stenting and post-stenting lumen and tortuosity.

Model label	Pre-stenting	*HI*	*HA*
Tortuosity	0.049	0.038 (−22.4%)	0.028 (−44.1%)
Lumen CCA [mm^2]	50.3	56.0 (11.4%)	59.2 (17.7%)
Lumen ICA [mm^2]	24	28.4 (18.2%)	47.7 (98.4%)

CCA, common carotid artery; ICA, internal carotid artery.

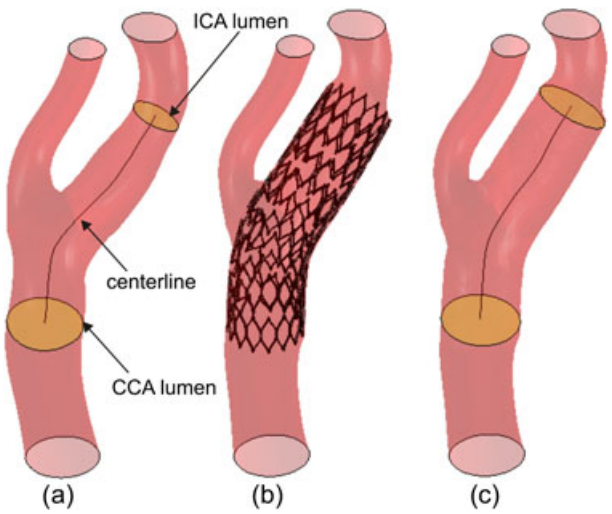

Figure 9. Representative illustration (model HA) of the (a) pre-stenting and (b) post-stenting lumen (pink), centerline (black) and considered vessel cross sections (yellow).

DOI: 10.1002/cnm

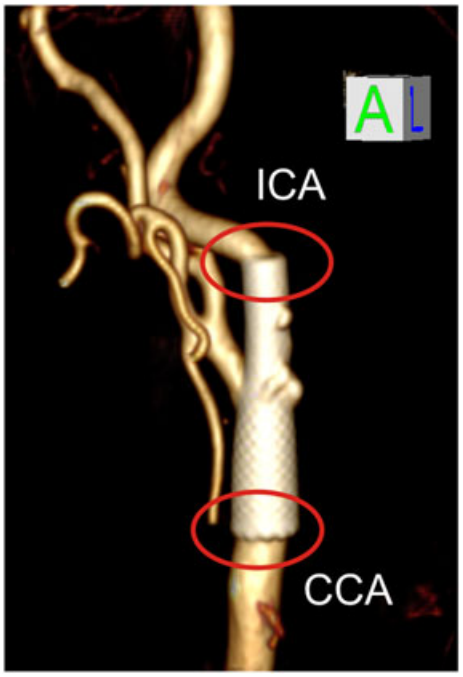

Figure 10. Three-dimensional reconstruction of post-stenting lumen from a computed tomography angiography. Red circles highlight the abrupt change of the lumen profile corresponding to the stent ends.

a part of real-time, computer-aided surgery planning applications is an appealing multidisciplinary research topic [47], which is further promoted by the dramatic enhancement of parallel computing and new medical imaging elaboration techniques.

4. LIMITATIONS

Although we have approached several issues regarding realistic simulation of CAS, this study has still some limitations to be addressed in future works.

In fact, we consider a carotid artery that does not show a significant stenosis, despite the presence of a plaque, as the vessel wall experiences positive remodeling (i.e., the vessel wall counteracts the plaque growth by outward enlargement to avoid lumen narrowing). In clinical practice, this case would not be considered for stenting [48], but, given the comparative nature of the present study, we consider this approach reasonable.

Even though a realistic morphology of the plaque is included in the CA model, we do not distinguish its components (e.g., lipid pool, necrotic core, calcific nodule, fibrous cap, etc.) to simplify the analysis. It is worth noting that, in the literature, several numerical studies include plaque components in the CA model [29, 42, 43], starting from high-resolution MRI images; however, we base our CA model on CTA as this imaging technique is currently used in the clinical practice to plan the CAS[§]. Although CTA can offer a high spacial resolution when compared with MRI, its drawback is that healthy wall thickness cannot be identified, and plaque characterization requires dedicated CT machine settings and reconstruction algorithms [49, 51, 52]. Consequently, because the outer boundary of the CA cannot be shown by CTA, we reconstruct it by appropriate hypotheses imposing a variable wall thickness along the CA model; as reported in Table A.1, the average wall thickness ranges from 1.5 to 0.9 mm for the ICA and from 1.7 to 1.1 mm for CCA. These values are congruent with the data reported by Astor *et al.* [53], who conclude the following: (i) atherosclerotic thickening

[§]For an overview on the role of medical imaging for diagnosis and treatment of CA stenosis, the reader should refer to [49, 50]

DOI: 10.1002/cnm

in the ICA appears to be accommodated for vessels with a maximum wall thickness of less than 1.5 mm; (ii) beyond this threshold, a greater thickness is associated with a smaller lumen; and (iii) the CCA appears to accommodate a wall thickness of less than 2.0 mm.

With respect to the constitutive modeling of the vessel tissue, it is worth highlighting that we base our model on fitting the data reported by Sommer *et al.* [24] on a single set of data (i.e., 0% axial stretch) for each test case (i.e., CCA/ICA wall). Clearly the consideration of a wider number of datasets and different levels of axial prestretch can influence the model fitting process providing thus different model coefficients [31]. A number of other aspects are also neglected, such as luminal blood pressure, axial pre-stretch, and residual stresses; in fact, we generate the vessel model moving basically from CTA images, which can provide a sort of snapshot of the lumen configuration in a certain instant of cardiac cycle. This configuration is related to the following: (i) residual stresses and (ii) *in vivo* loading caused by blood pressure. These two loading conditions are frequently referred to as pre-stress. A number of strategies, to take into account pre-stress, are available in literature (e.g., see recent papers of Alastruè *et al.* [54] and Gee *et al.* [55]) and, generally, each research group has his own strategy, but, in our opinion, the challenge of including realistic (patient-specific) pre-stress is not solved yet. Moreover, such a task in our case seems more challenging because we are dealing with non-homogeneous material due to plaque inclusion. A successful approach could exploit four-dimensional images, linking this configuration and loading change during the cardiac cycle [56]. Furthermore, in dealing with the contact, we adopt the general contact algorithm available in Abaqus/Explicit to take into account contact in the simulation because this approach allows simple definitions of contact with very few restrictions on the types of involved surfaces. By default, Abaqus assumes that the interaction between contacting bodies is frictionless. We keep this option because the choice of a friction coefficient (using for instance the basic Coulomb friction model) can not be fully motivated. In fact, to the best of our knowledge, there is a lack of concrete information about frictional parameters regarding stent/vessel interaction, as highlighted by Holzapfel *et al.* [57]. Different studies investigating stent/vessel interaction by FEA assume frictionless contact [17, 58]. Petrini *et al.* [59] and Wu *et al.* [19] assumed a friction coefficient of 0.05 between the stent and the artery in their simulation, whereas Mortier *et al.* [18] adopted a coefficient of 0.2. Only recently, Vad *et al.* [60] have investigated the determination of friction coefficient for self-expanding stent-grafts, which is anyway different from our case. Moreover, because we are investigating the stent apposition to the vessel wall, which is mainly due to stent radial expansion, the impact of the tangential component of the contact can be reasonably assumed negligible.

5. CONCLUSIONS

In the present study, we simulate CAS through patient-specific FEA; in particular, we focus on the influence of the constitutive vessel modeling on the simulation predictions with respect to stress distribution over the vessel wall, vessel straightening and lumen enlargement. Although both models indicate similar pattern with respect to the stress distribution, the introduction of fibers in the material model leads to a higher vessel straightening and a more evident discontinuity of the lumen area near the stent ends, as observed in the clinical practice.

Our results confirm the previous indications [41], which highlight that simplified isotropic constitutive models, even if well accepted in literature, should be carefully adopted, given the crucial dependency of simulation outcomes on the adopted vessel constitutive model and related material properties.

From a more general point of view, because FEA is nowadays a well-assessed technique to investigate the impact of stenting on the vessel wall, and given the rapid evolution of both medical imaging techniques and computational methods, the challenge of using FEA of CAS as a procedure planning tool supporting the clinical practice seems feasible. Following this idea and keeping the highlighted limitations in mind, the present study represents a further step toward a realistic simulation environment for CAS, which could be enhanced including the prestress of vessel wall and comparing the simulation results with a real CAS case, thus exploiting pre-operative and post-operative information.

DOI: 10.1002/cnm

APPENDIX A

A.1. Vessel wall thickness

Because no information on vessel wall thickness is obtainable from CTA images, we reconstruct the vessel wall outer profile, enlarging appropriately the inner sections, to maintain the plaque enclosed between the inner and outer profiles. In Table A.1 the obtained wall thickness, as a function of the CA sections, is reported.

A.2. Mesh convergence analysis

We performed a preliminary mesh-convergence analysis in order to assess the impact of the mesh density with respect to the following issues: (i) capability of the mesh generation procedure to capture the plaque morphology, that is, plaque volume; (ii) predicted vessel wall stress, that is, σ_M^{99P}.

Consequently, we created different CA models, with different mesh densities by varying two mesh parameters: (i) number of elements along wall thickness (EL_{th}) and (ii) number of elements along the cross-sectional circumference (EL_{circum}). It is necessary to highlight that the mesh-convergence analysis with respect to the plaque volume is purely geometrical as we refer to Δ_{Plaque} as the difference between the plaque volume predicted by the plaque element set and the volume ($\mathrm{Vol}_{\mathrm{ref}}$), enclosed into the STL surface derived from CTA scans.

The results reported in Table A.2 highlight that:

- fixing EL_{th} to 6, the increase of EL_{circum} from 42 to 62 has a negligible impact on both predicted plaque volume and $\sigma_M^{99\mathrm{P}}$;
- fixing EL_{circum} to 42, the increase of EL_{th} from 3 to 12 shows a plateau for considered output variables at $EL_{\mathrm{th}} = 9$.

Table A.1. Lumen radius and wall thickness for the ICA and CCA section highlighted in Figure 2. The values are reported for each section as mean ± standard deviation.

	ICA		CCA	
Section ID	Radius [mm]	Thickness [mm]	Radius [mm]	Thickness [mm]
1	3.4 ± 0.5	1.2 ± 0.6	3.9 ± 0.3	1.1 ± 0.0
2	3.3 ± 0.6	1.5 ± 0.7	3.8 ± 0.2	1.1 ± 0.0
3	2.8 ± 0.5	1.5 ± 0.7	4.0 ± 0.3	1.1 ± 0.0
4	2.8 ± 0.1	1.2 ± 0.5	3.9 ± 0.3	1.1 ± 0.0
5	2.7 ± 0.2	0.9 ± 0.0	3.9 ± 0.6	1.5 ± 0.7
6	2.8 ± 0.2	0.9 ± 0.0	4.8 ± 1.0	1.7 ± 0.5
7	2.8 ± 0.3	0.9 ± 0.0		

ICA, internal carotid artery; CCA, common carotid artery.

Table A.2. Mesh-convergence analysis with respect to the following: (i) number of elements along the wall thickness (EL_{th}) and (ii) number of elements along cross-sectional circumference (EL_{circum}). We indicate with Δ_{Plaque} the percentage difference between the actual predicted volume and the reference plaque volume $\mathrm{Vol}_{\mathrm{ref}}$, that is, 66.7 mm^3.

EL_{th}	EL_{circum}	N_{elems}	Δ_{elems}[%]	σ_M^{99P} [kPa]	Δ_σ[%]	$\mathrm{Vol}_{\mathrm{plaque}}$ $[\mathrm{mm}^3]$	Δ_{Plaque} [% $\mathrm{Vol}_{\mathrm{ref}}$]
6	42	39104	—	119.2	—	60.2	−9.8
6	50	46541	19.0	118.5	−0.6	60.7	−9.0
6	62	57725	47.6	118.5	−0.6	59.4	−10.9
3	42	19592	—	121.4	—	49.2	−26.3
6	42	39104	99.6	119.2	−1.8	60.2	−9.8
9	42	58666	199.4	117.8	−3.0	58.8	−11.9
12	42	78228	299.3	117.1	−3.5	58.8	−11.9

DOI: 10.1002/cnm

It is worth noting that Δ_{Plaque} converges to -11.9% for $EL_{\mathrm{th}} \geqslant 9$ and is minimally influenced by the increase of EL_{circum}. Because further mesh refining would dramatically increase the computational costs without improving sensibly both Δ_{Plaque} and Δ_{sigma}, we chose a final mesh defined by $EL_{\mathrm{th}} = 9$ and $EL_{\mathrm{circum}} = 42$.

The results suggest also further improvements of the strategy for plaque inclusion (Section 2.1) to enhance its accuracy.

A.3. Assigning local coordinate system for fiber orientation

In the following, we describe the adopted procedure to assign an appropriate local coordinate system to each element of the vessel mesh, as required for the implementation of the anisotropic hyperelastic model available in Abaqus.

If we consider the artery as a cylindrical tube, its geometry can be described by means of a cylindrical coordinate system defined by three unit vectors $\boldsymbol{e_1}, \boldsymbol{e_2}, \boldsymbol{e_3}$, which represent radial, circumferential and axial direction, respectively. Under this idealization, collagen fibers are supposed to be helically disposed with respect to the circumferential direction [25, 61]: in the undeformed configuration, the fiber orientations are locally defined by two unit vectors, $\boldsymbol{a_{01}}$ and $\boldsymbol{a_{02}}$, lying in the plane tangent to the cylindrical surface that contains the circumferential and the axial directions, $\boldsymbol{e_2}$ and $\boldsymbol{e_3}$. In this plane, the unit vectors $\boldsymbol{a_{01}}$ and $\boldsymbol{a_{02}}$ form constant angles $\pm\gamma$ with the circumferential direction. For this particular case, the components of the unit vectors $\boldsymbol{a_{01}}$ and $\boldsymbol{a_{02}}$, with respect to the cylindrical coordinate system $(\boldsymbol{e_1}, \boldsymbol{e_2}, \boldsymbol{e_3})$ are as follows:

$$\boldsymbol{a_{01}} = (0, \cos\gamma, \sin\gamma)\,, \qquad \boldsymbol{a_{02}} = (0, \cos\gamma, -\sin\gamma)\,. \tag{5}$$

Therefore, the definition of the fiber orientation is related to the definition of the local coordinate system $\boldsymbol{e_1}, \boldsymbol{e_2}, \boldsymbol{e_3}$ and γ.

The previous discussion can now be generalized to more complex geometries as a bifurcated vessel (Figure A.1(a)), where the centerline is defined as a sequence of segments (Figure A.1(b)); we consider, in our approach, each *segment k* of the centerline as the local axial axis ($\boldsymbol{e_3}$) of a corresponding set of the elements, *element set k*, assessed by the following steps:

1. for each *segment k* of the centerline, find the middle point M_k;
2. for each *element i* of the mesh:
   - compute the distance $\overline{G_i M_j}$ (j = 1:k);
   - assign the element to *element set k* corresponding to M_k minimizing $\overline{G_i M_j}$.

Then, for each *element i* of *element set k*, the local basis $\boldsymbol{e_1}, \boldsymbol{e_2}, \boldsymbol{e_3}$ is defined as follows:

- Axial axis, $\boldsymbol{e_3}$: this vector has the same orientation of the *segment k* defined by the points a_k and b_k of the centerline;
- Radial axis, $\boldsymbol{e_1}$: this vector lies in the plane defined by points G_i, a_k, b_k and is perpendicular to $\boldsymbol{e_3}$; thus, $\boldsymbol{e_1}$ has the direction of the segment $\overline{G_i H_k}$;
- Tangential axis, $\boldsymbol{e_2}$: this vector is obtained by computing the vector product $\boldsymbol{e_3} \times \boldsymbol{e_1}$.

Clearly, the three vectors $\boldsymbol{e_1}, \boldsymbol{e_2}, \boldsymbol{e_3}$ have to be normalized. Finally, the basis $\boldsymbol{e_1}, \boldsymbol{e_2}, \boldsymbol{e_3}$ are properly rotated according to the orientation of the element (Figure A.1(c)); this procedure is then iteratively applied to identify a local cylindrical coordinate system for each element of the mesh (Figure A.1(d)). Given the local basis, the fiber orientation for each element is given by Equation (5). We remark that this procedure was implemented for brick-like elements or four-node planar elements, but it can easily be adapted to triangular or tetrahedral meshes.

DOI: 10.1002/cnm

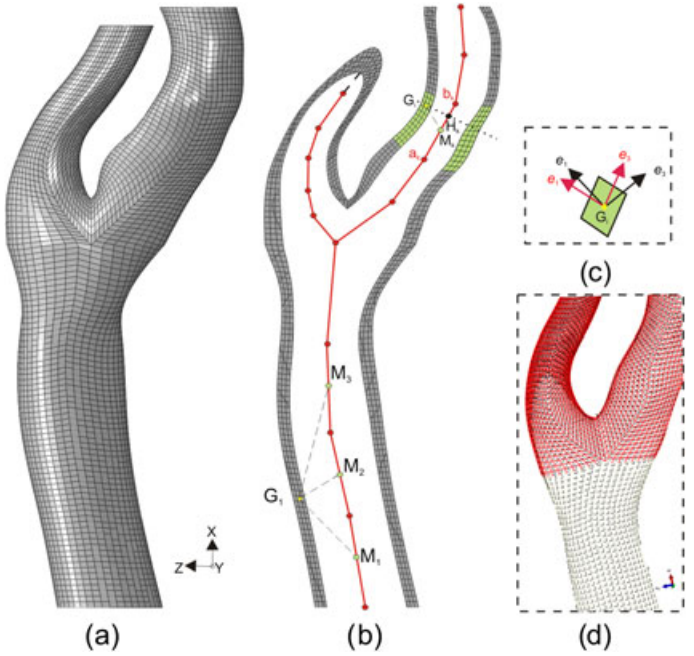

Figure A.1. (a) Mesh of the carotid artery model; (b) example of local coordinate system definition; (c) local cylindrical coordinate system rotation to accomplish element orientation; and (d) obtained collagen fiber distribution (circumferential and axial direction) at bifurcation for common carotid artery (white) and internal carotid artery/external carotid artery (red).

Other procedures to automatically define the distribution of collagen fibers for models of vascular structures have been reported in the literature, Basically, they can be classified in two categories, depending on the following facts: (i) the fiber orientation is defined with a local coordinate system and (ii) the fiber direction is estimated through a remodeling procedure, and hence the local coordinate system is defined by the principal stress/strain directions pre-computed using an isotropic model for the vessel wall [44, 54, 62–65].

As discussed, our approach belongs to the first category as well as the study of Kiousis *et al.* [43] and Mortier *et al.* [18].

A.4. Computational cost

We performed a scalability test for a benchmark analysis simulating the stent deployment within CA model. The model is composed of 108,744 elements and 192,084 nodes leading to 576,252 unknowns. ABQ/EXP 6.9 (Simulia Inc.) is the adopted solver; we ran the test on the *lagrange* cluster, available at Cilea (Segrate, Milan) and composed by 208 nodes having eight cores per node. The cluster is configured as follows:

- CPU: Intel Xeon X5460 QuadCore 3.166 GHz;
- RAM: 16 GB per node;
- Interconnections: Infiniband DDR (20 GB/s)

The results indicated that optimizing the hardware use is possible to finalize the analysis in 11 h using eight CPUs; the use of additional CPUs does not provide significant elapsed time speed-up. Although very far from the ideal on-fly response, the test highlighted that it is feasible to execute an analysis in an acceptable time to support procedure planning. In fact, usually 1 week is the time elapsed between the diagnostic imaging and CAS performance.

The impact of the adopted material model in the simulation duration is limited. In fact, Abaqus/Explicit uses a central difference rule to integrate the equations of motion explicitly through time. The stability limit Δt_{stable} of the integration scheme depends on the characteristic element

DOI: 10.1002/cnm

length and the dilatation wave speed c_d, which is function of material properties and density ρ. The time increment Δt used in an analysis must be smaller than the stability limit of the central-difference operator; this Δt drives the analysis duration. In our simulations, the most critical elements conditioning the minimum Δt belong to stent mesh, consequently, both analyses have similar Δt. Moreover, the most striking feature of the explicit method is the absence of a global tangent stiffness matrix, which is required with implicit methods. Because the state of the model is explicitly advanced, iterations and tolerances are not required, and this issue further reduces the impact of the adopted material model in the simulation duration. Because the state of the model is explicitly advanced, there are no iterations to be performed and tolerances to be checked. This issue further reduces the impact of the adopted material model on the simulation duration. In particular, to confirm it, we run a test-analysis, that is, a simple tension of strip cut along axial direction proposed as benchmark files in the Abaqus Documentation (3.1.7 Anisotropic hyperelastic modeling of arterial layers), fixing all the analysis parameters except the constitutive model. The CPU time required to perform the test with model HA was only 4.5% higher than its HI counterpart.

ACKNOWLEDGEMENTS

This work is funded by Cariplo Foundation through the Project no. 2009.2822 and ERC Starting Grant through the Project *ISOBIO: Isogeometric Methods for Biomechanics* (no. 259229).

The authors would like to acknowledge Dr. R. Dore, Prof. A. Odero, and Dr. S. Pirrelli of IRCCS Policlinico S. Matteo, Pavia, Italy for their support on medical aspects related to the present work; Eng. D. Van Loo of Ghent University (UGCT), Ghent, Belgium for micro-CT scanning of stent samples; CILEA, Interuniversity Consortium (Milan, Italy), through the LISA project BIO-FSI, for providing computational facilities.

REFERENCES

1. CREST committee. Stenting versus endarterectomy for treatment of carotid-artery stenosis. *New England Journal of Medicine* 2010; **363**:11–24.
2. Serruys P, Kutryk M, Ong A. Coronary-artery stents. *New England Journal of Medicine* 2006; **354**:483–495.
3. Gröschel K, Riecker A, Schulz J, Ernemann U, Kastrup A. Systematic review of early recurrent stenosis after angioplasty and stenting. *Stroke* 2005; **36**:367–373.
4. Henry M, Henry I, Klonaris C, Masson I, Hugel M, Tzvetanov K, Ethevenot G, Le BE, Kownator S, Luizi F, *et al.* Benefits of cerebral protection during carotid stenting with the percusurge guardwire system: midterm results. *Journal of Endovascular Therapy* 2002; **9**:1–13.
5. Christiaans M, Ernst J, Suttorp M, van den Berg J, Overtoom T, Kelder J, Mauser H, Ackerstaff R, Antonius Carotid Endarterectomy, Angioplasty, and Stenting Study Group. Restenosis after carotid angioplasty and stenting: a follow-up study with duplex ultrasonography. *European Journal of Vascular and Endovascular Surgery* 2003; **26**:141–144.
6. Bosiers M, Peeters P, Deloose K, Verbist J, Sievert H, Sugita J, Castriota F, Cremonesi A. Does carotid artery stenting work on the long run: 5-year results in high-volume centers (ELOCAS Registry). *Journal of Cardiovascular Surgery (Torino)* 2005; **46**:241–247.
7. De Donato G, Setacci C, Deloose K, Peeters P, Cremonesi A, Bosiers M. Long-term results of carotid artery stenting. *Journal of Vascular Surgery* 2008; **48**:1431–1441.
8. Steinbauer MGM, Pfister K, Greind M, Schlachetzki F, Borisch I, Schuirer G, Feuerbach S, Kasprzak P. Alert for increased long-term follow-up after carotid artery stenting: results of a prospective, randomized, single-center trial of carotid artery stenting vs carotid endarterectomy. *Journal of Vascular Surgery* 2008; **48**:93–98.
9. Harrer J, Morschel R, Mull M, Kosinski C. High rate of restenosis after carotid artery stenting in patients with high-grade internal carotid artery stenosis. *Journal of Neurology* 2008; **255**:1309–1314.
10. Nolz R, Schernthaner R, Cejna M, Schernthaner M, Lammer J, Schoder M. Carotid artery stenting: single-center experience over 11 years. *CardioVascular and Interventional Radiology* 2010; **33**:251–259.
11. Edelman E, Rogers C. Pathobiologic response to stenting. *American Journal of Cardiology* 1998; **81**:4E–6E.
12. Schwartz R, Huber K. Restenosis and the proportional neointimal response to coronary artery injury: results in a porcine model. *Journal of the American College of Cardiology* 1992; **19**:267–274.
13. Kornowski R, Hong M, Tio F, Bramwell O, Wu H, Leon M. In-stent restenosis: contributions of inflammatory responses and arterial injury to neointimal hyperplasia. *Journal of the American College of Cardiology* 1998; **31**:224–230.
14. Auricchio F, Di Loreto M, Sacco E. Finite element analysis of a stenotic artery revascularization through stent insertion. *Computer Methods in Biomechanics and Biomedical Engineering* 2001; **4**:249–263.

DOI: 10.1002/cnm

15. Lally C, Dolan F, Prendergast P. Cardiovascular stent design and vessel stresses: a finite element analysis. *Journal of Biomechanics* 2005; **38**:1574–1581.
16. Kiousis D, Gasser C, Holzapfel G. A numerical model to study the interaction of vascular stents with human atherosclerotic lesions. *Annals of Biomedical Engineering* 2007; **11**:1857–1869.
17. Gijsen F, Migliavacca F, Schievano S, Socci L, Petrini L, Thury A, Wentzel J, van der Steen A, Serruys P, Dubini G. Simulation of stent deployment in a realistic human coronary artery. *BioMedical Engineering OnLine* 2008; **7**:1–11.
18. Mortier P, Holzapfel G, De Beule M, Van Loo D, Taeymans Y, Segers P, Verdonck P, Verhegghe B. A novel simulation strategy for stent insertion and deployment in curved coronary bifurcations: comparison of three drug-eluting stents. *Annals of Biomedical Engineering* 2010; **38**:88–99.
19. Wu W, Qi M, Liu XP, Yang DZ, Wang WQ. Delivery and release of nitinol stent in carotid artery and their interactions: a finite element analysis. *Journal of Biomechanics* 2007; **40**:3034–3040.
20. Conti M, Auricchio F, De Beule M, Verhegghe B. Numerical simulation of nitinol peripheral stents: from laser-cutting to deployment in a patient specific anatomy. *Proceeding of ESOMAT 2009*, Prague, 2009; 1–6, DOI: 10.1051/esomat/200906008.
21. Auricchio F, Conti M, De Beule M, De Santis G, Verhegghe B. Carotid artery stenting simulation: from patient-specific images to finite element analysis. *Medical Engineering & Physics* 2011; **33**:281–289.
22. Conti M, Van Loo D, Auricchio F, De Beule M, De Santis G, Verhegghe B, Pirrelli S, Odero A. Impact of carotid stent cell design on vessel scaffolding: a case study comparing experimental investigation and numerical simulations. *Journal of Endovascular Therapy* 2011; **18**:397–406.
23. Mortier P, De Beule M, Van Loo D, Verhegghe B, Verdonck P. Atherosclerotic lesion mechanics versus biology. *Zeitschrift für Kardiologie* 2000; **89**:S080–S084.
24. Sommer G, Regitnig P, Koltringer L, Holzapfel G. Biaxial mechanical properties of intact and layer-dissected human carotid arteries at physiological and supraphysiological loadings. *American Journal of Physiology - Heart and Circulatory Physiology* 2009; **298**:H898–912.
25. Holzapfel G, Gasser T, Ogden R. A new constitutive framework for arterial wall mechanics and a comparative study of material models. *Journal of Elasticity* 2000; **61**:1–48.
26. Gasser T, Ogden R, Holzapfel G. Hyperelastic modelling of arterial layers with distributed collagen fibre orientations. *Journal of the Royal Society Interface* 2006; **3**:15–35.
27. Rosset A, Spadola L, Ratib O. Osirix: an open-source software for navigating in multidimensional dicom images. *Journal of Digital Imaging* 2004; **17**:205–216.
28. Creane A, Maher E, Sultan S, Hynes N, Kelly DJ, Lally C. Finite element modelling of diseased carotid bifurcations generated from *in vivo* computerised tomographic angiography. *Computers in Biology and Medicine* 2010; **40**:419–429.
29. Gao H, Long Q. Effects of varied lipid core volume and fibrous cap thickness on stress distribution in carotid arterial plaques. *Journal of Biomechanics* 2008; **41**(14):3053–3059.
30. Tang D, Yang C, Kobayashi S, Ku N. Effect of a lipid pool on stress/strain distributions in stenotic arteries: 3D fluid-structure interactions (FSI) models. *Journal of Biomechanical Engineering* 2004; **126**:363–370.
31. Sommer G. *Mechanical Properties of Healthy and Diseased Human Arteries: Insights into Human Arterial Biomechanics and Related Material Modeling*, Monographic Series TU Graz, Computation in Engineering and Science. Verlag der Technischen Universität Graz: Graz, Austria, 2010.
32. Maher E, Creane A, Sultan S, Hynes N, Lally C, Kelly D. Tensile and compressive properties of fresh human carotid atherosclerotic plaques. *Journal of Biomechanics* 2009; **16**:2760–2767.
33. Simulia. *Abaqus Manual*. Dassault Systèmes: Providence, RI, USA, 2009.
34. Rebelo N, Walker N, Foadian H. Simulation of implantable stents. *Abaqus User's Conference* 2001; **143**:421–434.
35. Auricchio F, Taylor R. Shape-memory alloys: modeling and numerical simulations of the finite-strain superelastic behavior. *Computer Methods in Applied Mechanics and Engineering* 1996; **143**:175–194.
36. Auricchio F, Taylor R. Shape-memory alloys: macromodeling and numerical simulations of the superelastic behavior. *Computer Methods in Applied Mechanics and Engineering* 1997; **146**:281–312.
37. Kleinstreuer C, Li Z, Basciano CA, Seelecke S, Farber MA. Computational mechanics of nitinol stent grafts. *Journal of Biomechanics* 2008; **41**:2370–2378.
38. Thomas J, Antiga L, Che S, Milner J, Hangan Steinman D, Spence J, Kutt B, Steinman D. Variation in the carotid bifurcation geometry of young versus older adults: implications for geometric risk of atherosclerosis. *Stroke* 2005; **36**:2450–2456.
39. Capelli C, Gervaso F, Petrini L, Dubini G, Migliavacca F. Assessment of tissue prolapse after balloon-expandable stenting: influence of stent cell geometry. *Medical Engineering & Physics* 2009; **31**:441–447.
40. Pericevic I, Lally C, Toner D, Kelly DJ. The influence of plaque composition on underlying arterial wall stress during stent expansion: the case for lesion-specific stents. *Medical Engineering & Physics* 2009; **31**:428–433.
41. Holzapfel G, Stadler M, Schulze-Bauer C. A layer-specific three-dimensional model for the simulation of balloon angioplasty using magnetic resonance imaging and mechanical testing. *Annals of Biomedical Engineering* 2002; **30**:753–767.
42. Tang D, Teng Z, Canton G, Yang C, Ferguson M, Huang X, Zheng J, Woodard P, Yuan C. Sites of rupture in human atherosclerotic carotid plaques are associated with high structural stresses: an in vivo MRI-based 3D fluid-structure interaction study. *Stroke* 2009; **40**:3258–3263.

DOI: 10.1002/cnm

43. Kiousis D, Rubinigg S, Auer M, Holzapfel G. A methodology to analyze changes in lipid core and calcification onto fibrous cap vulnerability: the human atherosclerotic carotid bifurcation as an illustratory example. *Journal of Biomechanical Engineering* 2009; **131**:121002(9 pages).
44. Hariton I, deBotton G, Gasser TC, Holzapfel G. Stress-modulated collagen fiber remodeling in a human carotid bifurcation. *Journal of Theoretical Biology* 2007; **248**:460–470.
45. Delfino A, Stergiopulos N, Moore J, Meister J. Residual strain effects in the stress field in a thick wall finite element model of the human carotid bifurcation. *Journal of Biomechanics* 1997; **30**:777–786.
46. Clark D, Lessio S, O'Donoghue M, Tsalamandris C, Schainfeld R, Rosenfield K. Mechanisms and predictors of carotid artery stent restenosis: a serial intravascular ultrasound study. *Journal of the American College of Cardiology* 2006; **47**:2390–2396.
47. project) RF. Real time simulation for safer vascular stenting, 2012. (Available from: http://www.rt3s.eu, [Accessed on February 1, 2012]).
48. Bates E. ACCF/SCAI/SVMB/SIR/ASITN 2007 Clinical expert consensus document on carotid stenting. *Journal of the American College of Cardiology* 2007; **49**:126–170.
49. Gillard J, Graves M, Hatsukami T, Yuan C. *Carotid Disease, The Role of Imaging in Diagnosis and Management*. Cambridge University Press: UPH, Shaftesbury Road, Cambridge, CB2 8BS, United Kingdom, 2007.
50. Maldonado TS. What are current preprocedure imaging requirements for carotid artery stenting and carotid endarterectomy: have magnetic resonance angiography and computed tomographic angiography made a difference? *Seminars in Vascular Surgery* 2007; **20**(4):205–215.
51. de Weert T, Ouhlous M, Meijering E, Zondervan P, Hendriks J, van Sambeek M, Dippel D, van der Lugt A. *In vivo* characterization and quantification of atherosclerotic carotid plaque with components with multidetector computed tomography and histopathological correlation. *Arteriosclerosis, Thrombosis, and Vascular Biology* 2006; **26**:2366–2372.
52. de Weert T, Ouhlous M, Zondervan P, Hendriks J, Dippel D, van Sambeek M, van der Lugt A. *In vitro* characterization of atherosclerotic carotid plaque with multidetector computed tomography and histopathological correlation. *European Radiology* 2005:1906–1914.
53. Astor BC, Sharrett AR, Coresh J, Chambless LE, Wasserman BA. Remodeling of carotid arteries detected with MR imaging: atherosclerosis risk in communities carotid MRI study1. *Radiology* 2010; **256**(3):879–886. DOI: 10.1148/radiol.10091162.
54. Alastruè V, Garica A, Pena E, Rodriguez J, Martinez M, Doblare M. Numerical framework for patient-specific computational modelling of vascular tissue. *International Journal for Numerical Methods in Biomedical Engineering* 2010; **26**:35–51.
55. Gee M, Förster C, Wall W. A computational strategy for prestressing patient-specific biomechanical problems under finite deformations. *International Journal for Numerical Methods in Biomedical Engineering* 2010; **26**:52–72.
56. Perego M, Veneziani A, Vergara C. A variational approach for estimating the compliance of the cardiovascular tissue: an inverse fluid-structure interaction problem. *SIAM Journal of Scientific Computing* 2011; **33**:1181–1211.
57. Holzapfel G, Stadler M, Gasser T. Changes in the mechanical environment of the stenotic arteries during interaction with stents: computational assessment of parametric stent design. *Journal of Biomechanical Engineering* 2005; **127**:166–180.
58. Early M, Lally C, Prendergast P, Kelly D. Stresses in peripheral arteries following stent placement: a finite element analysis. *Computer Methods in Biomechanics and Biomedical Engineering* 2009; **12**:25–33.
59. Petrini L, Migliavacca F, Massarotti P, Schievano S, Dubini G, Auricchio F. Computational studies of shape memory alloy behavior in biomedical applications. *Journal of Biomechanical Engineering* 2005; **127**:716–725.
60. Vad S, Eskinazi A, Corbett T, McGloughlin T, Geest JPV. Determination of coefficient of friction for self-expanding stent-grafts. *Journal of Biomechanical Engineering* 2010; **132**(12):121007.
61. Holzapfel G, Sommer G, Regitnig P. Anisotropic mechanical properties of the tissue components in human atherosclerotic plaques. *Journal of Biomechanical Engineering* 2004; **126**:657–665.
62. Driessen N, Cox M, Bouten C, Baaijens F. Remodelling of the angular collagen fiber distribution in cardiovascular tissues. *Biomechanics and Modeling in Mechanobiology* 2008; **7**:93–103.
63. Driessen N, Wilson W, Bouten C, Baaijens F. A computational model for collagen fibre remodelling in the arterial wall. *Journal of Theoretical Biology* 2004; **226**:53–64.
64. Hariton I, deBotton G, Gasser T, Holzapfel G. Stress-driven collagen fiber remodeling in arterial walls. *Biomechanics and Modeling in Mechanobiology* 2007; **6**:163–175.
65. Hariton I, deBotton G, Gasser TC, Holzapfel GA. How to incorporate collagen fibers orientations in an arterial bifurcation? In *Proceedings of the 3rd IASTED International Conference on Biomechanics*, Hamza MH (ed.). ACTA Press: Anaheim, 2005; 101–104.

DOI: 10.1002/cnm